

# Journal of Geophysical Research: Solid Earth

## RESEARCH ARTICLE

10.1002/2013JB010278

**Key Points:**

- Observe localized zones with high-amplitude reflections off Massachusetts
- Full-waveform inversion and 1D fluid flow modeling to understand overpressure
- Focused fluid flow from Pleistocene glaciations sources localized overpressure

**Correspondence to:**B. Dugan,  
dugan@rice.edu**Citation:**

Siegel, J., D. Lizarralde, B. Dugan, and M. Person (2014), Glacially generated overpressure on the New England continental shelf: Integration of full-waveform inversion and overpressure modeling, *J. Geophys. Res. Solid Earth*, 119, doi:10.1002/2013JB010278.

Received 15 APR 2013

Accepted 3 MAR 2014

Accepted article online 10 MAR 2014

## Glacially generated overpressure on the New England continental shelf: Integration of full-waveform inversion and overpressure modeling

**Jacob Siegel<sup>1</sup>, Daniel Lizarralde<sup>2</sup>, Brandon Dugan<sup>1</sup>, and Mark Person<sup>3</sup>**

<sup>1</sup>Department of Earth Science, William Marsh Rice University, Houston, Texas, USA, <sup>2</sup>Department of Geology and Geophysics, Woods Hole Oceanographic Institution, Woods Hole, Massachusetts, USA, <sup>3</sup>Department of Earth and Environmental Sciences, New Mexico Institute of Mining and Technology, Socorro, New Mexico, USA

**Abstract** Localized zones of high-amplitude, discontinuous seismic reflections 100 km off the coast of Massachusetts, USA, have  $P$  wave velocities up to 190 m/s lower than those of adjacent sediments of equal depth (250 m below the sea floor). To investigate the origin of these low-velocity zones, we compare the detailed velocity structure across high-amplitude regions to adjacent, undisturbed regions through full-waveform inversion. We relate the full-waveform inversion velocities to effective stress and overpressure with a power law model. This model predicts localized overpressures up to 2.2 MPa associated with the high-amplitude reflections. To help understand the overpressure source, we model overpressure due to erosion, glacial loading, and sedimentation in one dimension. The modeling results show that ice loading from a late Pleistocene glaciation, ice loading from the Last Glacial Maximum, and rapid sedimentation contributed to the overpressure. Localized overpressure, however, is likely the result of focused fluid flow through a high-permeability layer below the region characterized by the high-amplitude reflections. These high overpressures may have also caused localized sediment deformation. Our forward models predict maximum overpressure during the Last Glacial Maximum due to loading by glaciers and rapid sedimentation, but these overpressures are dissipating in the modern, low sedimentation rate environment. This has important implications for our understanding continental shelf morphology, fluid flow, and submarine groundwater discharge off Massachusetts, as we show a mechanism related to Pleistocene ice sheets that may have created regions of anomalously high overpressure.

## 1. Introduction

Continental shelf sediments often contain large regions with pore pressure above hydrostatic pressure (overpressure). These overpressures are often formed by a combination of rapid sedimentation, fluid expansion and migration, and/or phase changes [Bredehoeft and Hanshaw, 1968; Bethke and Corbet, 1998; Hart et al., 1995; Gordon and Flemings, 1998; Swarbrick and Osborne, 1998; Dugan et al., 2003]. Understanding and locating overpressure is important as it can affect subsurface fluid flow, submarine groundwater discharge (SGD), compaction and deformation of sediments, slope stability, offshore drilling strategies, fracture formation, and fluid migration pathways [e.g., Roberts and Nunn, 1995; Gordon and Flemings, 1998; Dugan and Flemings, 2002; Dugan and Sheahan, 2012]. Thus, an accurate understanding of overpressure is central to our understanding of offshore fluid flow regimes and their influence on some continental shelf processes.

Wells drilled on the New England continental shelf, beneath Nantucket Island, documented unexpected overpressure (7 to 8 m above average sea level) within aquifers that are several hundred meters below sea level (Figure 1). This overpressure cannot be produced by the low, local fluvial sedimentation rates and sediment properties in the region [Marksamer et al., 2007]. The overpressure may be a relic of Pleistocene sea level rise and fall and ice sheet loading [Person et al., 2007]. The continental margin off Massachusetts was repeatedly glaciated throughout the late Pleistocene [Oldale and O'Hara, 1984; Uchupi et al., 2001; Siegel et al., 2012]. Two- and three-dimensional paleohydrologic models simulate how these glacial cycles, in combination with sea level fluctuations, had a strong influence on the offshore hydrogeologic system [Person et al., 2003; Marksamer et al., 2007; Cohen et al., 2010]. In particular, the models show that these glaciation cycles may have emplaced large volumes of subsurface freshwater tens of kilometers beyond the edge of the ice sheets [Person et al., 2003; Marksamer et al., 2007; Cohen et al., 2010]. A glacial influence on this hydrogeologic system may also explain low-salinity groundwater observed on Nantucket Island [Folger et al., 1978]. However, there are currently no direct

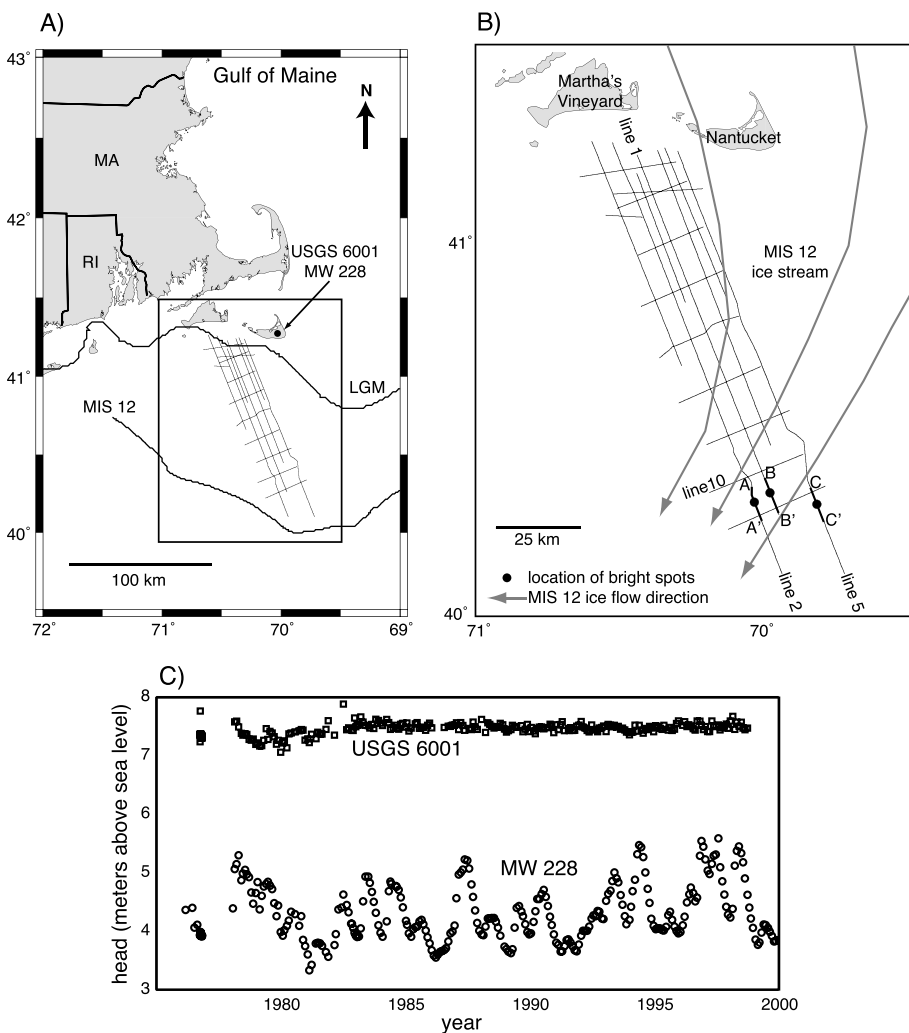


**Figure 1.** (a) Regional base map showing location of seismic lines used in this study along with the location of the maximum extent of the last glacial maximum (line labeled LGM) [Uchupi et al., 2001] and the inferred maximum extent of a MIS 12 ice sheet (black line labeled MIS 12) [Siegel et al., 2012]. The box shows the location of Figure 1b. (b) Detailed map showing the location of the seismic lines used in this study along with the location of bright spots observed in the lines (marked with dots). Gray lines show the direction of ice flow for the MIS 12 ice stream. All of the bright spots are approximately located within a trough formed by a paleo-ice stream [Siegel et al., 2012]. (c) Measured head data comparing shallow water table head in Nantucket well 228 (circles) and head within deeper Cretaceous aquifers in U.S. Geological Survey well 6001 (squares). The comparison of the data shows that the aquifers are not related and that the deeper Cretaceous aquifer has anomalously higher pressure, which is interpreted to be glacial in origin [Marksamer et al., 2007].

observations that verify the existence or constrain the extent of the overpressure due to glaciation on the continental shelf predicted by numerical models.

A high-resolution, multichannel, seismic data set collected on the continental shelf off Massachusetts shows several regions of localized, relatively high amplitude, disturbed sediments (bright spots) directly above a marine oxygen isotope stage (MIS) 12 glacial erosion surface [Siegel et al., 2012] (Figures 1 and 2). Siegel et al. [2012] show that the continental shelf off Massachusetts was glaciated in the late Pleistocene. Marksamer et al. [2007] show that the Last Glacial Maximum (LGM) may have increased overpressure tens of kilometers beyond the maximum extent of the Laurentide ice sheet. We suggest that the bright spots observed in the seismic data could be regions of localized overpressure generated during late Pleistocene glaciations. To evaluate this possibility, we determine the detailed (2–4 m resolution) vertical velocity structure through the seismic bright spots using a full-waveform inversion approach. We then determine overpressure based on

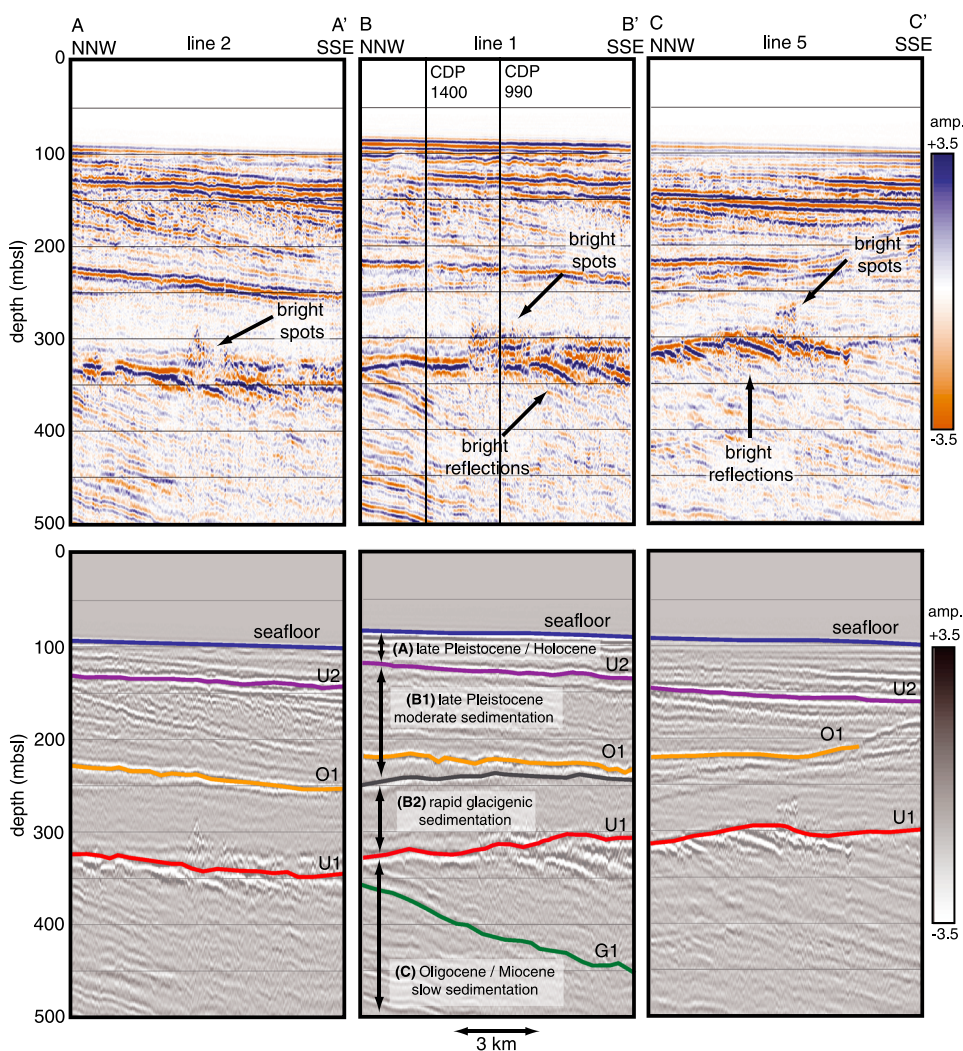


**Figure 2.** (top) Seismic sections that contain bright spots and bright dipping reflections (locations are indicated in Figure 1b). (bottom) Same seismic sections plotted in grayscale with major reflections and interpreted sediment history marked. The interpreted sediment history is from Siegel *et al.* [2012]. U1 is an MIS 12 glacial unconformity formed by an ice stream. The bright spots overlie the U1 unconformity and are contained within a 50–75 m thick glaciogenic sediment unit that was deposited during ice stream retreat [Siegel *et al.*, 2012]. Scale bars on the right show relative amplitude for the seismic data.

the seismic velocities using an empirical relationship between effective stress and  $P$  wave velocity [Bowers, 1995]. We compare this velocity-predicted overpressure to overpressure predicted from one-dimensional (1-D) forward models that include ice sheet loading, erosion, and sedimentation. Our comparison shows that the observed changes in velocities in the bright spots can be explained by localized overpressures that developed from focused fluid flow via permeable pathways due to ice sheet loading from late Pleistocene ice sheets or rapid sedimentation during LGM ice sheet retreat. Our results thus provide observations to support the predictions of modeling studies that suggest a strong influence of glaciation on modern offshore overpressure [Person *et al.*, 2003; Marksamer *et al.*, 2007; Cohen *et al.*, 2010] while also suggesting that stratigraphy and fluid flow play a role.

## 2. Geologic Setting

The continental shelf off Massachusetts is part of a passive margin that was initiated by rifting during the breakup of Pangea and the opening of the Atlantic during the Late Triassic to Early Jurassic. After breakup, the margin continued to subside and to fill with sediments from the Cretaceous to the present, forming a thick

sedimentary wedge overlying Jurassic basement [Hutchinson *et al.*, 1986]. The base of the sedimentary wedge consists of a thick package of Cretaceous to Eocene carbonate mud [Steckler *et al.*, 1999]. During the Oligocene and Miocene, siliciclastic sedimentation increased nearly twentyfold, and there was a pronounced shift from primarily aggrading sediments to prograding siliciclastic clinoforms (Unit C in Figure 2) [Steckler *et al.*, 1999]. The Miocene clinoforms likely graded from mud prone at the base to silt prone at the top [Siegel *et al.*, 2012], consistent with lithologic trends observed in Oligocene and Miocene clinoforms off New Jersey [Greenlee *et al.*, 1992].

The MIS 12 glacial unconformity (unconformity U1 in Figure 2) marks the onset of Pleistocene shelf-crossing glaciations off Massachusetts and the location of an ice stream that was sourced from the Gulf of Maine [Siegel *et al.*, 2012]. The ice stream eroded a trough, 100 m deep and 50 km wide, into the underlying Oligocene/Miocene sediments. During ice stream retreat, a 50–100 m thick deposit of glacigenic sediments, which likely consisted of poorly sorted silts and clays, was rapidly deposited proglacially (Unit B2 in Figure 2). Several subsequent glacial cycles terminated on the shelf throughout the remainder of the late Pleistocene, including the LGM, which terminated near Martha's Vineyard and Nantucket islands (Figure 1) [Oldale and O'Hare, 1984; Uchupi *et al.*, 2001]. High sediment input during the Pleistocene, combined with sea level changes, produced a series of prograding clinoforms (Unit B1 in Figure 2). During the last sea level fall (40–30 ka), a shallow sequence boundary was formed (unconformity U2 in Figure 2) that is overlain by a combination of late Pleistocene and Holocene siliciclastic sediments [Siegel *et al.*, 2012].

### 3. Data Description and Observations

Our geophysical data set consists of a series of high-resolution, multichannel seismic (MCS) lines collected off Massachusetts (Figures 1a and 1b) with the Scripps Institution of Oceanography's portable seismic system. The source was a 45 cubic inches/105 cubic inches ( $737.5 \text{ cm}^3/1720.6 \text{ cm}^3$ ) generator-injector air gun that produces frequencies up to 200 Hz. The nominal shot spacing was 12.5 m. The streamer consisted of 48 channels with a group spacing of 12.5 m, a near offset of 50 m, and a far offset of 650 m. The data were sorted into common depth point (CDP) bins spaced every 6.25 m, yielding an average CDP fold of 24 channels.

We observe bright spots and bright dipping reflections in several seismic lines within the glacigenic sediments of Unit B2 directly above the glacial unconformity (U1) at 300–350 m below sea level (bsl) (Figures 1 and 2). Unconformity U1 is the remnant of an ice stream trough (Figure 1b). The trend of the bright spots is approximately perpendicular to the flow direction of the ice stream and follows the strike of clinoforms in the underlying Miocene stratigraphic unit (Unit C in Figure 2). The bright spots have a semidisturbed seismic character and have relatively higher amplitude compared to adjacent sedimentary units. Discernable reflections within the bright spots, however, correlate with adjacent reflections in the glacigenic sediments just outside the bright spots. The dipping reflections within the underlying Miocene strata also have relatively higher amplitudes that are localized to several tens of meters below the U1 glacial unconformity just below the bright spots (bright dipping reflections in Figure 2).

The enhanced reflectivity of the bright spots and underlying dipping reflections is unlikely to be due to the presence of either free gas or gas hydrate. An association of the bright spots with gas hydrate can be ruled out as methane gas hydrate is not stable at these depths [e.g. Xu and Ruppel, 1999; Phrampus and Hornbach, 2012]. The presence of free gas, perhaps trapped beneath the unconformity, also seems unlikely based on the lack of frequency-dependent amplitude loss below the bright spots, as would be expected if free gas were present [White, 1975; Taylor *et al.*, 2000; Morgan *et al.*, 2012]. This is demonstrated in Figure 3, where spectral lines and notches are shifted for data beneath the bright spots relative to the rest of the section, but spectral slopes are unchanged. Interval velocities in the region of the bright spots are lower than in the rest of the section (Figure 4), which could indicate the presence of free gas, but the magnitude of the velocity anomaly (100 m/s) is less than what would be expected if free gas were present [Domenico, 1976; Ecker *et al.*, 2000]. For the remainder of this paper we explore an alternative explanation for the origin of the bright spots that is consistent with their distribution and the history of shelf glaciation.

### 4. Full-Waveform Inversion

Full-waveform inversion is a modeling tool that estimates detailed velocity structure by predicting the full prestack seismic wavefield [Minshull *et al.*, 1994; Sain *et al.*, 2000; Virieux and Operto, 2009]. We analyze our

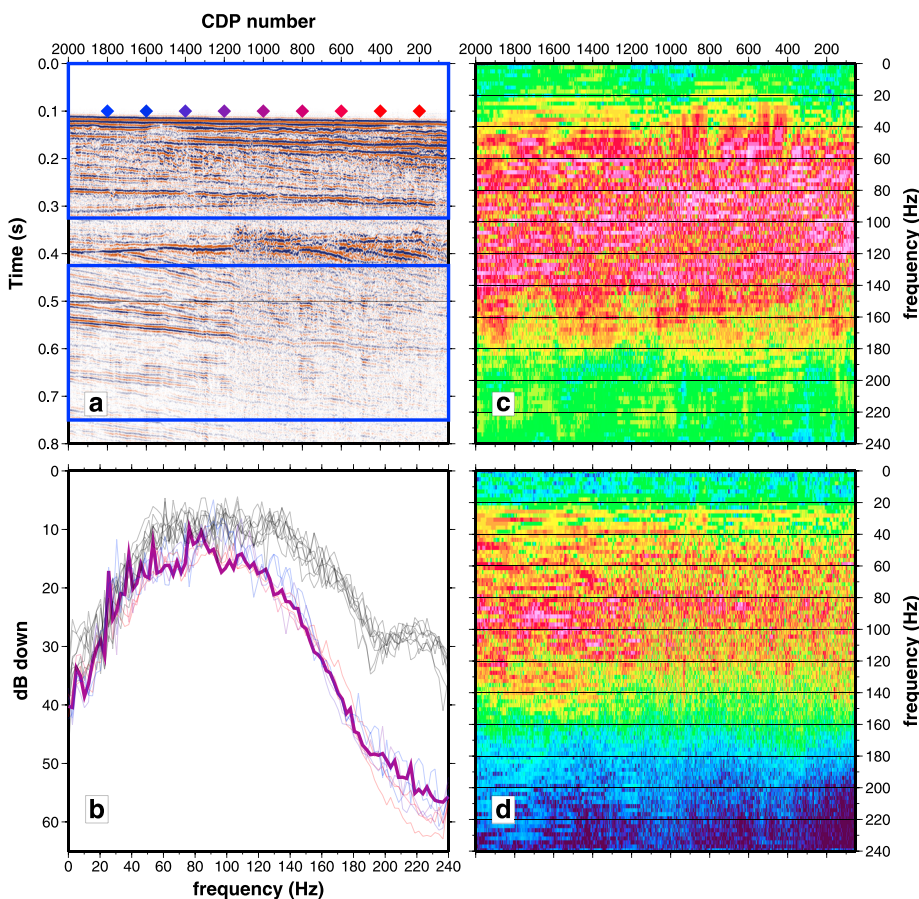


**Figure 3.** (a) Seismic section with blue boxes indicating CDP/time ranges over which spectra in Figures 3b–3d are calculated. (b) Colored curves: average spectra each for 200 CDPs centered on the colored diamond locations in Figure 3a; for example, position 1000 (plotted with a thicker curve) is the average of spectra for CDPs 900–1100 for the time interval 0.425–0.750 s; black curves are average spectra for 200 CDPs centered on the diamond locations within the upper box in Figure 3a, 0–0.325 s. (c) Spectra for every CDP calculated for the time range 0–0.325 s (the upper box in Figure 3a). (d) Spectra for every CDP calculated for the time range 0.425–0.750 s (the lower box in Figure 3a). All spectra are plotted as decibels down from the maximum power in Figure 3c. The effect of a lateral change in anelastic attenuation would appear as a change in spectral slope with frequency, with a steeper slope for higher attenuation regions. This effect is not observed.

data set using the linearized waveform inversion approach of Kormendi and Dietrich [1991]. This type of analysis has been extensively described in the literature, and our particular approach closely follows that of Korenaga *et al.* [1997], so we have placed details of our analysis in Appendix A.

#### 4.1. Starting Model

The full-waveform inversion algorithm solves for best fit models ( $m$ ) that are linearly close to the starting model ( $m_0$ ), i.e., solving for short-wavelength velocity perturbations. An accurate inversion result thus requires a starting model that captures the long- to intermediate-wavelength subsurface velocity structure such that reflection traveltimes are accurately predicted. We use a weighted, damped, least squares inversion to solve for a smooth starting velocity model based on picked normal moveout (NMO) stacking velocities in the seismic data [Lizarralde and Swift, 1999]. A smooth inversion seeks to minimize the change in velocity with depth, and it creates a model that varies slowly and penalizes rapid change in velocity. NMO velocities were picked every 125 m on prominent horizons that are correlated through the seismic section and are spaced an average 100 ms apart in time. Three to five adjacent, smoothed interval velocity profiles were averaged and used as the starting model in the inversion process (Figure 4).

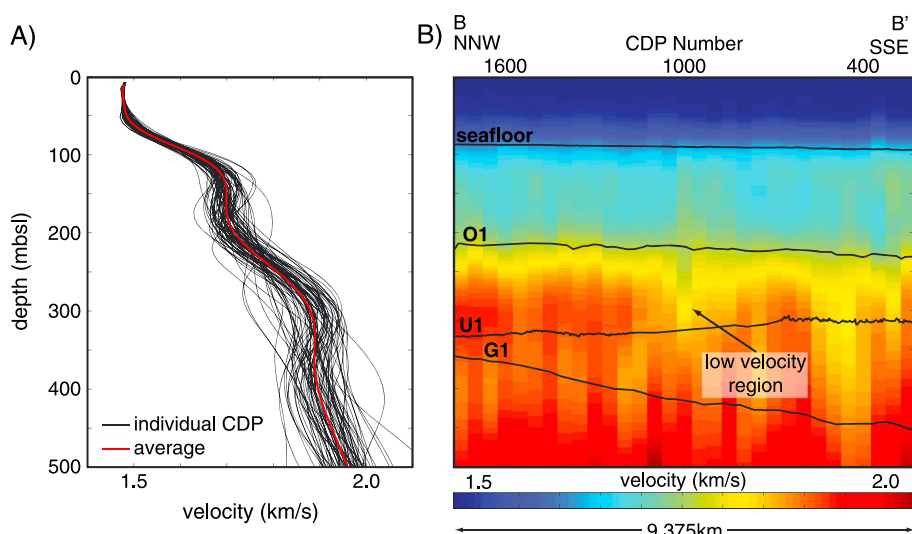


**Figure 4.** (a) Smooth interval velocities for all CDPs interpreted across the part of seismic line 1 containing bright spots and the average interval velocity. (b) Color map plot of the interval velocities averaged every fifth CDP. This is the same section of seismic line 1 shown in Figure 2 (location is indicated in Figure 1b). Most interval velocities are similar; however, there is a noticeable reduction in the velocities between CDPs 800–1100, particularly CDP 1000. The low-velocity region is approximately co-located with the location of the bright spots. The interval velocities are the starting model for the full-waveform inversion.

#### 4.2. Sensitivity Tests

We want to use differences between adjacent velocity profiles, determined from full-waveform inversion, to make inferences on overpressure. It is thus important to have estimates of the uncertainties in these modeled velocity functions. We estimate model uncertainties by testing sensitivity to two main sources of error in the inversion: failure of the 1-D assumption (accuracy) and robustness (precision), which is a function of the inversion's sensitivity to small deviations in the data, potentially due to noise.

We assess the effect of dip on accuracy by comparing full-waveform inversion results from colocated CDPs at the intersection of perpendicular lines 1 and 10 (Figure 1). Reflection dips range between  $0^\circ$  and  $1^\circ$  toward the south-southeast in the depth interval of interest ( $0$ – $500$  m bsl), with a marked increase in dip below the glacial unconformity (U1). The velocities obtained from the full-waveform inversions display a similar pattern, particularly above the U1 unconformity (Figure 5a), where both the amplitude and the phase of the velocity/depth functions agree well. Dip introduces both a velocity error and a depth error into the velocity estimate of a particular stratal unit. A simple difference of the two velocity functions thus overestimates the velocity difference of individual units by including both the velocity and depth errors due to dip via the misalignment of the peaks and troughs in the velocity profiles. To separate these two effects of dip, we cross correlate the two velocity/depth profiles, applying an 80 m long, tapered window centered at each depth point and align each point of the two velocity/depth profiles based on the maximum cross-correlation values so that velocity differences between the same stratal units can be compared. The cross-correlation lags, or depth shift required to maximize cross correlation at each depth, are thus a measure of depth uncertainty as a function of depth (Figure 5b), and the difference in inverted velocity between the aligned profiles (Figure 5c) is a measure of velocity uncertainty as a function of depth. Above the unconformity, where reflection dips are low, depth differences between the two profiles are 1 m or less and velocity differences average 15.6 m/s with a maximum difference of 49.0 m/s (2.5%). Below the unconformity, where reflection dip is highest ( $0.5^\circ$ – $1.0^\circ$ ), the average velocity difference increases to 26.3 m/s, with a maximum difference of 74.5 m/s (3.7%), and depth differences increase to 4–6 m. Despite this deviation, the apparent pattern of velocity variation is similar on both lines. In addition, the bright spots are located above the glacial unconformity where dip is lower and therefore has less error.

We concentrate on the result of the full-waveform inversion through two contrasting regions of seismic line 1. CDP 990 traverses the center of the region containing the bright spots, whereas CDP 1400 traverses a section 2.5 km to the north-northwest that does not contain bright spots, yet contains similar stratigraphy (Figures 2 and 6). For both

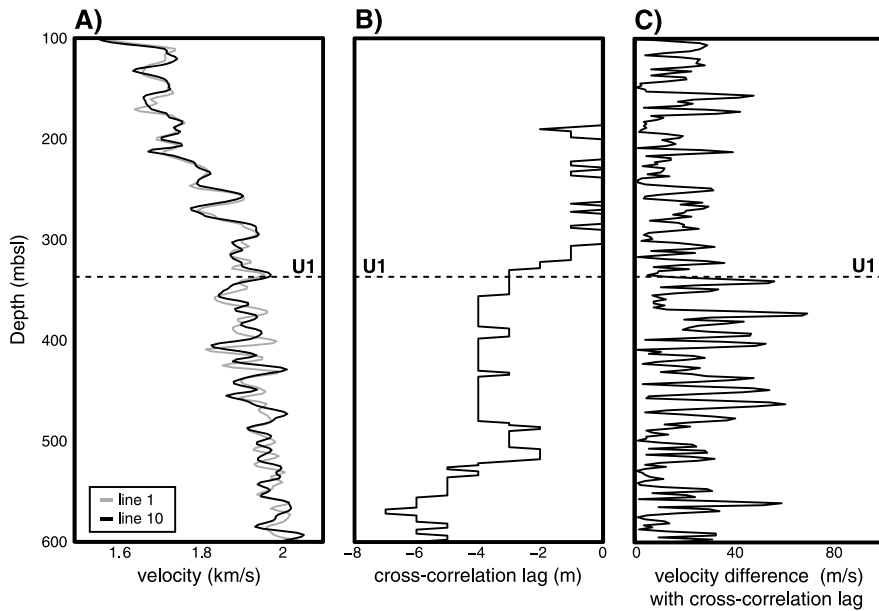


**Figure 5.** (a) Full-waveform inversion velocity results for colocated CDPs on crossing lines to test the effects of dip with our assumption of 1-D velocity inversion. Line 1 is shown in gray, and line 10 is shown in black. (b) Cross-correlation lag with depth based on an 80 m window. (c) The difference in velocity between the two full-waveform inversion results when the velocity profiles are shifted by their cross-correlation lag. The difference is largest just below the unconformity (U1) where there is the steepest dip in reflections (Figure 2).

CDP locations, the full-waveform inversion was run on three adjacent CDPs to help quantify the precision of the final velocity model (Figure 6). The predicted velocities of adjacent CDPs are similar, with a standard error (standard deviation of the mean) between 0.0 and 32.5 m/s for CDP 990 (average 5.2 m/s) and 0.0 and 19.1 m/s for CDP 1400 (average 6.7 m/s). The error tends to increase below the bright reflection of the glacial unconformity (U1). This is due to higher dips.

The synthetic waveform traces generated with the final 1-D stratified Earth model closely match the observed seismic data for the range in  $p$  values used in the inversion (Figure 7). The waveform fit is worse at large  $p$  values for the U1 reflection at CDP 990. This may be due to the effect of dip, an overly coarse grid spacing, or an inappropriate parameterization of  $V_s$  and density. However, the fit at all values of  $p$  is good over the time interval corresponding to the bright spots, which display a clear increase in amplitude with increasing  $p$  for CDP 900 that is well fit by the model (Figure 7).

#### 4.3. Results

The final velocity model for the CDP group is defined as the average of the three adjacent CDPs (Figure 6). The final velocity models show similar patterns that correlate with the observed stratigraphy (Figure 8). Sediments just below the seafloor and the O1 reflection have lower velocities, whereas the U1 reflection corresponds to a large velocity increase in both profiles. This indicates that sediment properties are consistent across the seismic section and produce correspondingly similar velocity patterns. The velocity of the bright spots, however, are  $190 \pm 80$  m/s lower than adjacent sediments at the same depth without bright spots (Figures 6 and 8). This observed velocity difference is larger than the velocity differences of the starting models, the estimated uncertainties due to dip, and the inherent precision of the approach. We note that the velocity reduction of 190 m/s (~10%) in the region of the bright spots is small relative to velocity reductions predicted due to even a fraction of a percent of free gas in sediments at these depths [Domenico, 1976]. We thus explore overpressure as a mechanism for velocity reduction in the vicinity of the bright spots.

#### 5. Velocity-Predicted Overpressure

The velocity of a sedimentary rock in the subsurface is a function of many factors, including its depositional and burial history, lithology, texture, porosity, consolidation state, density, temperature, pore fluid type, and

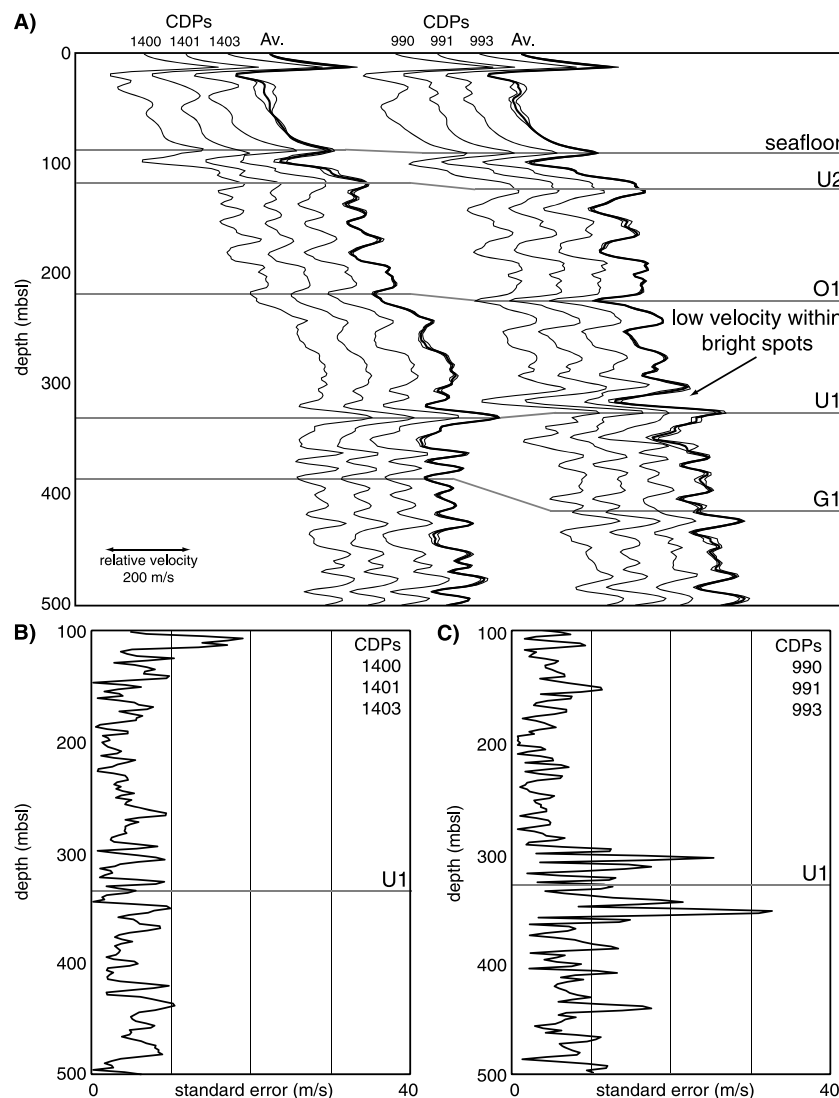


**Figure 6.** (a) Full-waveform inversion results for two CDP groups. CDP 1400 does not contain any bright spots, whereas CDP 990 goes through the middle of the bright spot region. Adjacent CDPs within the group all show similar velocity results. The average of the CDPs is shown in bold with the standard error represented by the thin black lines. (b and c) Standard error (standard deviation of the mean) of the two CDP groups.

overpressure [Bowers, 1995; Dutta, 2002; Dvorkin and Nur, 2002; Huffman, 2002]. In considering the cause of the abrupt lateral change in seismic velocity exhibited by the bright spots, abrupt changes in most of these factors can be discounted. The bright spots occur within a coherent unit characterized by uniformly low impedance everywhere except for the isolated, localized bright spots. This indicates that lithology is consistent across the unit. Moreover, the coherent unit is inferred to be backfilling, glaci fluvial sediments [Siegel et al., 2012], which were shown with well data to have consistent, similar lithology [Kristensen et al., 2008]. The velocity change could indicate porosity change. Empirical relationships that relate velocity to porosity [e.g., Marion et al., 1992; Erickson and Jarrard, 1998] predict a change in porosity of 0.05 (20% change in porosity), assuming an average porosity of 0.25 in the unit. However, this difference in porosity would not be expected given the sediment type and depositional history is consistent across the seismic section.

The bright spots are situated above an unconformity that truncates dipping reflections whose amplitudes are themselves anomalously bright in regions beneath the bright spots. This relationship strongly suggests a similar origin for their formation. As other first-order controls on velocity such as lithology and porosity are not likely, we explore the influence of overpressure on effective stress. We therefore assume that at a

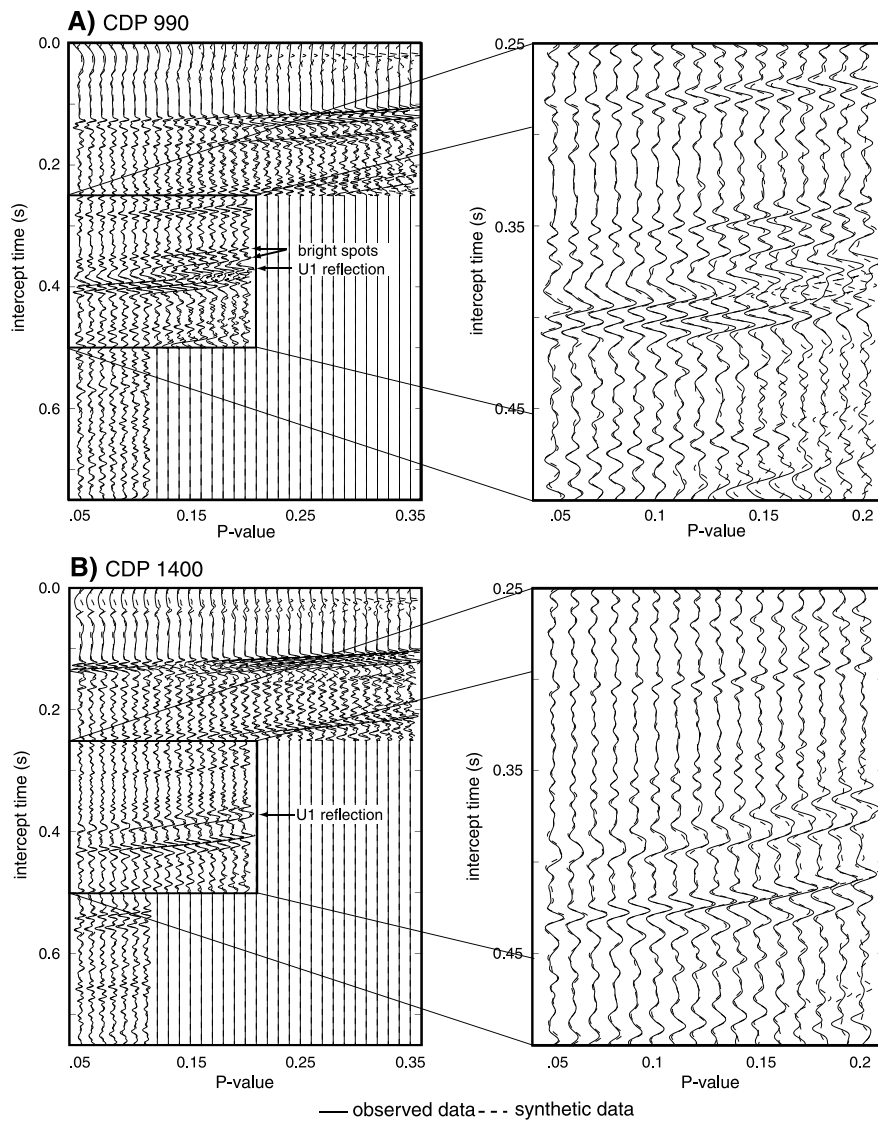


**Figure 7.** Results of full-waveform inversion for seismic line 1 CDPs 990 and 1400 in the  $\tau$ - $p$  domain showing the recorded seismic data (solid line) and synthetic seismic data based on the final 1-D stratified Earth model (dashed line). For lower  $p$  values, there is an excellent fit between the synthetic and the observed waveforms. The waveforms shown correspond to the full range of time and  $p$  values used for the inversion.

constant depth, observed velocity variations are most likely due to changes in effective stress, which are related to changes in overpressure and the bulk moduli of the materials [Carcione *et al.*, 2003]. Dutta [2002] and Bowers [2002] showed that, at a given depth, deviations in observed seismic velocity from that predicted from a normal compaction trend could be used as an indicator of overpressure.

There are several empirically derived methods that can be used to estimate overpressure from seismic velocity by quantifying the deviation of the observed seismic velocities from a normal velocity trend [Bowers, 1995; Sayers *et al.*, 2002; Mavko *et al.*, 2009]. We use the method of Bowers [1995], which relates effective vertical stress and velocity as

$$\sigma' = \left( \frac{V - V_0}{A} \right)^{1/c}, \quad (1)$$

where  $\sigma'$  is effective vertical stress ( $S_v P_{\text{pore}}$ ),  $V$  is the velocity at depth, and  $V_0$  is the velocity of unconsolidated, fluid-saturated sediment (1500 m/s).  $S_v$  is the lithostatic stress or total vertical stress,  $P_{\text{pore}}$  is the pore pressure,

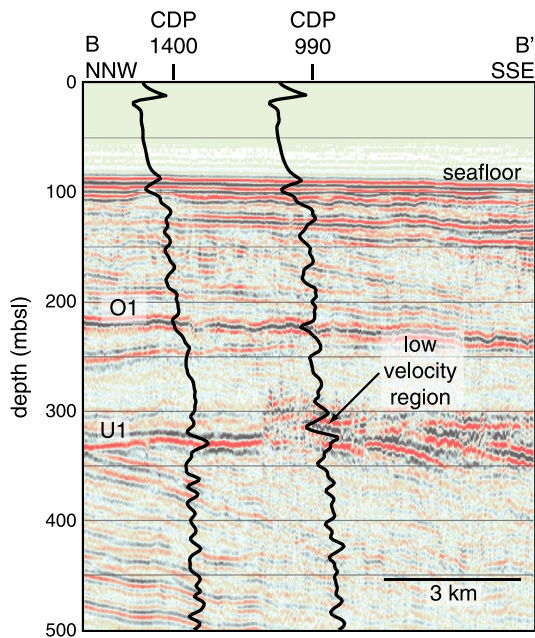


**Figure 8.** Overlay of full-waveform inversion velocity results on stacked section of seismic line 1.

express the change in pore pressure ( $dP$ ) given an observed change in velocity ( $dv$ ), we differentiate equation (1). The derivative of effective stress with respect to velocity is

$$\frac{d\sigma'}{dv} = \frac{d}{dv} (S_v - P_{\text{pore}}). \quad (2)$$

Lithostatic stress at any given depth is constant, and its derivative with respect to velocity is 0. Therefore, at a constant depth the change in effective stress with velocity relates to the change in pore pressure,

$$\frac{d}{dv} = -\frac{dP_{\text{pore}}}{dv}. \quad (3)$$

The right-hand side of equation (1) can be differentiated with respect to velocity and expressed as

$$\frac{d}{dv} \left( \frac{(v - v_0)^{(1/c)}}{A} \right) = \frac{\left( \frac{v - v_0}{A} \right)^{(1/c-1)}}{AC}. \quad (4)$$

The empirical estimate of change in pore pressure with respect to velocity is then

$$dP_{\text{pore}} = dv \frac{\left( \frac{v - v_0}{A} \right)^{(1/c-1)}}{AC}. \quad (5)$$

where  $dv$  is the change in velocity observed between CDPs at the location of the bright spots.

### 5.1. Results

We infer that the decrease in velocity of  $190 \pm 80$  m/s in the bright spots is due primarily to higher overpressure. Using equation (5), the change in velocity can be equated to a difference in overpressure of 0.9–2.2 MPa, given the estimated uncertainty in velocity at this depth and the range of scalar parameters  $A$  and  $C$ . Although there is a considerable range in the estimated overpressure differences, due primarily to uncertainties in  $A$  and  $C$ , even the minimum estimate represents a significant difference in highly localized overpressure.

Localized zones of relatively high overpressure could develop from a number of mechanisms, including (1) in situ fluid expansion; (2) rapid sedimentation; or (3) lateral pore pressure transfer [Swarbrick and Osborne, 1998; Bowers, 2002; Dugan and Sheahan, 2012]. Our study region has been repeatedly glaciated throughout the late Pleistocene, which can lead to sustained overpressures long after glacial retreat [Bense and Person, 2008].

and  $A$  and  $C$  are empirically derived constants that are unique to individual regions. We determine appropriate values for  $A$  and  $C$  via a grid search that seeks values which minimize the difference between the velocity trend predicted by equation (1) and the observed trend of average interval velocity (Figure 4). We use a range of possible effective stress trends appropriate for this location ranging from the minimum effective stress (near-lithostatic pore pressure) to maximum effective stress (near-hydrostatic pore pressure). For near-lithostatic pore pressure,  $A = 7.55$  and  $C = 0.29$ ; for near-hydrostatic pore pressure,  $A = 0.7$  and  $C = 0.44$ .

We use equation (1) to estimate differences in the effective stress across the seismic section given an observed difference in velocity within the bright spots compared to other regions that are assumed to follow an interpreted normal velocity trend. From the interpreted change in effective stress, we predict the corresponding change in pore pressure, which is equivalent in magnitude to the change in overpressure because the hydrostatic pressure is constant at any given depth below sea level. To

Given the glacial history in the region, the location of the bright spots just above the MIS 12 glacial unconformity, and their trend along strike of the underlying sedimentary unit, we suggest that the late Pleistocene ice sheets were the likely source of overpressure and explore this possibility with a simple 1-D fluid flow model.

## 6. One-Dimensional Fluid Flow Model

To investigate physical mechanisms that could explain the localized overpressure within the bright spots, we employ a 1-D, finite-difference, fluid flow model that solves the groundwater flow equation accounting for glacial loading, erosion, and sedimentation. We use a layered 1-D model to represent an idealized transect through the seismic section (Figure 2) that contains corresponding lithologic units and erosion surfaces to 1000 m bsl. The model space is discretized with an evolving grid that has a node spacing of 1 m.

### 6.1. Fluid Flow

We solve a 1-D equation for groundwater flow similar to ones solved by *Person et al.* [2007] and *Marksamer et al.* [2007] that incorporates ice sheet loading, erosion, and sedimentation,

$$K_z \frac{\partial^2 h}{\partial z^2} = S_s \left[ \frac{\partial h}{\partial t} - \zeta \frac{\rho_i}{\rho_f} \frac{\partial \eta}{\partial t} - \zeta \frac{\rho_b - \rho_w}{\rho_f} \frac{\partial L}{\partial t} - P_{ext} \right], \quad (6)$$

where  $K_z$  is the hydraulic conductivity in the vertical direction,  $h$  is hydraulic head relative to a reference datum of current sea level (0.0 m),  $S_s$  is the specific storage,  $\rho_i$ ,  $\rho_w$ , and  $\rho_b$  are the densities of ice, water, and fluid-saturated sediment,  $\eta$  and  $L$  are the elevations of the ice and sediment relative to sea level, respectively, and  $P_{ext}$  is an external source term that can be assigned to a particular layer to represent external fluid sources outside the model domain [Dugan and Germaine, 2008]. The coefficient  $\zeta$  in equation (6) is the 1-D loading efficiency, which defines the proportion of surface loading that is transferred to subsurface overpressure [Ingebretsen et al., 2007; Lemieux et al., 2008]. This is similar to the three-dimensional pore pressure buildup coefficient ( $B$ ) defined by Green and Wang [1986] as the change in pore pressure per unit change in applied stress. The exact value of  $\zeta$  depends on material properties such as bulk sediment and fluid compressibilities, which we approximate to estimate the general trend of  $\zeta$  during loading and unloading. During sediment and ice loading, when the bulk compressibility is orders of magnitude larger than fluid (water) compressibility,  $\zeta$  is generally close to a value of 1; thus, during loading in our model,  $\zeta$  is set to 0.95. This means much of the increase in overburden leads to a proportional increase in pore pressure. During sediment and ice sheet unloading, we assume compressibility is 10% of the initial compressibility [Corbet and Bethke, 1992; Stigall and Dugan, 2010], which results in a decrease in  $\zeta$ ; thus, during unloading in our model,  $\zeta$  is set to 0.50. This allows glacial overpressure to persist after the ice sheet has retreated.

We solve equation (6) using a fully implicit finite-difference approach [Fletcher, 1997]. The base of the model is a no-flow boundary, and the top boundary is set to be equivalent to either sea level or the head at the base of the ice sheet when the ice sheet is present; this is consistent with basin-scale models that account for ice sheet loading [e.g. *Person et al.*, 2007]. Many studies have modeled additional effects of ice sheets on fluid flow such as flexure of the crust and the formation of permafrost [Person et al., 2007; Bense and Person, 2008; Lemieux et al., 2008]; because we are only concerned with a 1-D model, and our study region is near the edge of the ice sheet, we do not account for flexure. Permafrost can reduce the permeability beneath and beyond the extent of the ice sheet. However, because our study region is in a paleo-ice stream trough that exhibited signs of basal melting via subglacial drainage channels [Siegel et al., 2012], permafrost would not likely develop.

Hydrostatic pressure ( $P_{hydro}$ ) is always assumed relative to sea level (which is constant in the model) and defined as

$$P_{hydro} = \rho_w g z, \quad (7)$$

where  $g$  is the acceleration due to gravity and  $z$  is the depth below sea level. Lithostatic stress ( $S_v$ ) is the stress from the overlying water, saturated sediment matrix, and ice sheet when present. Lithostatic stress is defined as

$$S_v = \int_0^z \rho_b g dz. \quad (8)$$

### 6.2. Model Domain

We simulate four distinct geologic stages consistent with the sedimentation and glacial history determined by *Siegel et al.* [2012] (Figure 9): (1) low-sedimentation rate during the Oligocene and Miocene; (2) glacial erosion and loading by the MIS 12 ice stream that increases in height to 500 m over a 20 kyr time period; (3)

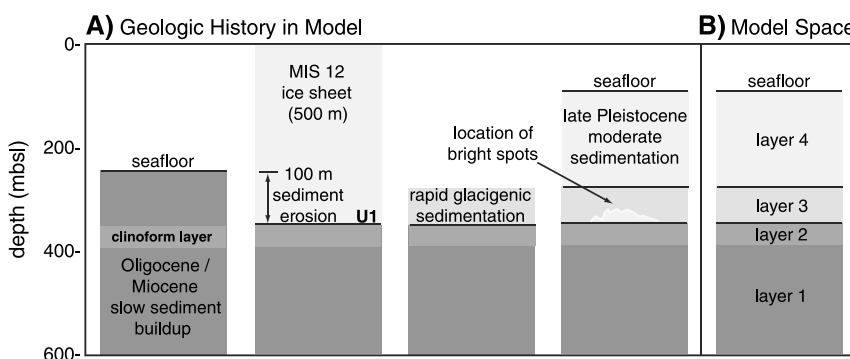


**Figure 9.** (a) Conceptual drawing showing the stratigraphic evolution (from left to right) of the seismic section that is used for the 1-D numerical model. (b) One-dimensional model space that is based on observed stratigraphy. Layer 1 in model extends to a depth of 1000 m bsl.

deglaciation and high sedimentation rate at the end of MIS 12 during a 10 kyr time period; and (4) moderate sedimentation rate during the late Pleistocene. The 1-D model contains four homogeneous layers to represent this geologic history (Figure 9). Layer 1 is an Oligocene/Miocene layer. Layer 2 is a 10 m thick, high-permeability layer below the U1 unconformity that represents a dipping clinoform that was eroded by the ice stream and continues down dip outside of the model space. Layer 3 is a glacigenic sediment layer. Layer 4 is a Pleistocene/Holocene layer.

The petrophysical properties we assign to each model layer are based on a combination of available well data and the properties of similar hydrogeologic units used in published hydrogeologic modeling studies of this area. On the New England continental shelf, fine-grained sediments range in permeability from  $10^{-10}$  to  $10^{-18} \text{ m}^2$  [Cohen et al., 2010], whereas clayey silts have an average permeability of  $10^{-16.5} \text{ m}^2$  [Person et al., 2003]. Glacigenic sediments such as till can have permeability of  $10^{-16} \text{ m}^2$  or lower [Keller et al., 1989]. Glaciolacustrine deposits on Nantucket were found to have a permeability of  $10^{-15} \text{ m}^2$  [Person et al., 2012]. Within the range of these possible permeability values, we assign permeability to each model layer that best produces the general trend of overpressure we estimate from the velocity model. The permeability values we use for the Oligocene/Miocene layer, the clinoform layer, the glacigenic layer, and the Pleistocene/Holocene layer are  $10^{-18}$ ,  $10^{-17}$ ,  $10^{-18}$ , and  $10^{-16} \text{ m}^2$ , respectively. A specific storage of  $5.0 \times 10^{-3} \text{ m}^{-1}$  was assigned to all layers.

### 6.3. Results

Based on the seismic velocities, we infer localized, higher overpressure of up to 2.2 MPa in the region of the bright spots compared to adjacent regions of the seismic section at the same depth (250 m bsl) and to underlying and overlying sediment layers. A series of numerical models were run to evaluate mechanisms that could explain the localized overpressure inferred within the bright spots, which are located within the glacigenic sediment layer. Glacial loading by an ice sheet during MIS 12, rapid sedimentation during glacial retreat, and moderate sedimentation during the Pleistocene all contribute to overpressure throughout the 1-D model space (Figure 10). The trend and magnitude of the overpressure is affected by the permeability architecture, the assumed thickness and duration of the MIS 12 ice sheet, and the timescale of glacigenic sedimentation during ice sheet retreat. However, in a 1-D model space, these variables cannot adequately create a localized zone of relatively higher overpressure within the glacigenic sediments compared to underlying or overlying units as predicted by the seismic velocities. Thus, an additional mechanism beyond a 1-D ice sheet and sediment loading is needed to generate localized, higher overpressure within the glacigenic sediment layer.

## 7. Discussion

### 7.1. Sources of Localized Overpressure

Additional sources of overpressure from outside the 1-D model domain may lead to localized regions of overpressure by the lateral migration of fluid through permeable pathways. This is commonly referred to as flow focusing [Yardley and Swarbrick, 2000; Flemings et al., 2002; Dugan and Flemings, 2002; Dugan and Sheahan, 2012]. Based on the orientation of the bright spots along strike of the dipping Miocene layers, we infer they are all related to the same clinoform, which could have high permeability (light gray clinoform

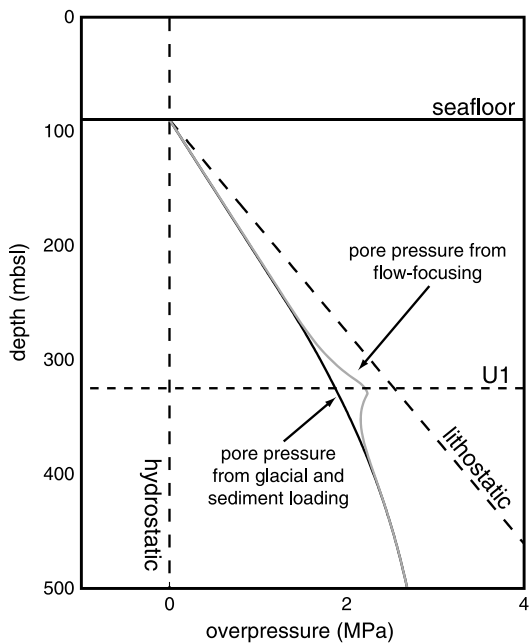


**Figure 10.** Results of the 1-D numerical modeling show the general trend in overpressure (solid black line) that is produced from ice sheet loading and sedimentation. The overpressure that is produced by lateral pore pressure transfer (solid gray line) shows the resulting increase in overpressure above and below the glacial unconformity.

near the shelf edge during LGM glacial retreat. When the additional source term is assigned to the clinoform layer during the LGM, localized (higher than the overlying or underlying layer) overpressure develops in the glaciogenic sediments and the clinoform layer, centered on the U1 unconformity. The model-predicted overpressure is approximately where the full-waveform inversion velocities predict the largest region of localized overpressure (i.e., in the bright spots, which are located within the glaciogenic sediments). Thus, the assumption of an additional overpressure source within the clinoform layer in the 1-D fluid flow model is the best match to the velocity-predicted overpressure. High overpressure in the underlying clinoform could also be creating the large impedance contrasts in the bright dipping layers (Figure 2).

Alternatively, the bright spots may be the result of fluid expulsion from underlying overpressured layers generated by the MIS 12 ice sheet as it retreated, and glaciogenic sediments were rapidly deposited (Figure 11b). Deformation is more likely near the ice sheet margin, where there is typically the highest gradient in subsurface overpressure from ice sheet loading due to the abrupt changes in ice sheet thickness

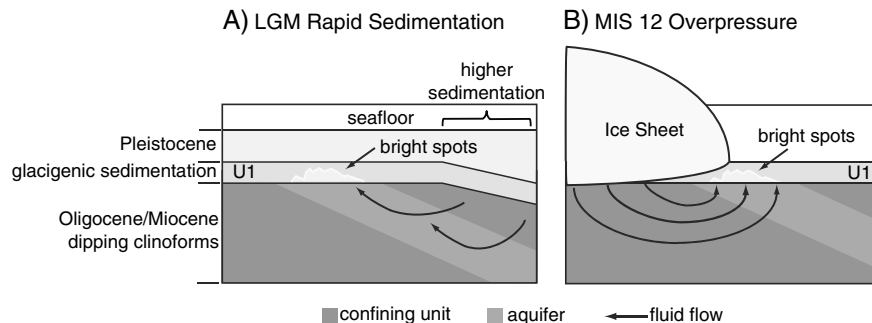


**Figure 11.** Conceptual drawing showing the potential to migrate overpressures generated from (a) rapid sedimentation during the LGM and (b) pore pressure from the MIS 12 ice sheet which also may have resulted in deformation features.

within the Oligocene/Miocene unit, Figure 11). That particular high-permeability clinoform could facilitate fluid migration from down dip where overpressure is interpreted to be higher. We consider two mechanisms that may be sources of overpressure outside our 1-D model domain: (1) overpressure generated on the continental shelf from LGM ice sheet loading and rapid sedimentation near the continental slope (Figure 11a) [Marksamer *et al.*, 2007] and (2) overpressure generated shoreward, where ice overburden and subsequently overpressure buildup were greater, which could migrate and increase overpressure near the ice margin where there was less ice overburden (Figure 11b) [Boulton *et al.*, 1993; Boulton and Caban, 1995; Bense and Person, 2008; Iverson and Person, 2012].

To evaluate the role of an external overpressure source linked with a high-permeability clinoform (Figure 11), we include a pressure source term ( $P_{ext}$  in equation (6)) in the high-permeability unit just below the unconformity (Layer 2 in Figure 9b). The external pressure source is specified to be 1.5 MPa for a period of 10 kyr, a similar magnitude of overpressure to that predicted near the shelf edge by Marksamer *et al.* [2007] due to higher sedimentation rates

[Iverson and Person, 2012]. Boulton and Caban [1995] showed that overpressure generated beyond the edge of an ice sheet can lead to flow focusing in regions where there is a break in a confining unit or permafrost; they noted that these geologic conditions can create fluid expulsion features, referred to as extrusion moraines, and can lead to a release of glacially generated overpressure into the overlying strata. Roberts and Nunn [1995] also showed that overpressure can build to a point where fractures occur, and fluid is rapidly expelled into overlying sediments. The bright spots may be the remnants of an expulsion feature created by this overpressure where flow was facilitated through a permeable clinoform (Figure 11b). This mechanism could also explain the semidisturbed seismic character of the bright spots.

These results demonstrate that flow focusing from late Pleistocene glacially generated overpressure is a possible mechanism for the localized overpressure and possible sediment deformation features observed in our seismic data. Overpressures encountered in deep aquifers (500 m bsl) on Nantucket are also interpreted to be related to overpressures generated during the LGM via lateral pressure transfer [Marksamer et al., 2007]. Together, these results highlight that regional sedimentation rate, stratigraphy, and glacial history are all important factors for understanding the occurrence and distribution of overpressure along this previously glaciated margin.

## 7.2. Implications for Submarine Groundwater Discharge

Large submarine groundwater discharge (SGD) fluxes have been inferred off New England from the  $^{228}\text{Ra}$  inventory in the upper ocean [Moore et al., 2008; Moore, 2010]. The overpressures predicted by our full-waveform inversion and numerical modeling could be the mechanism driving fluid flow linked to this SGD. Overpressure is a primary driving force for offshore groundwater flow [Dugan and Sheahan, 2012] and thus has a strong control on SGD. Understanding and characterizing SGD is important as it is an integral part of the total nutrient flux to the oceans, which affects marine biological production [Johannes, 1980; Church, 1996; Slomp and Cappellen, 2004]. Biological production, in turn, is a significant carbon sink in the global exogenic carbon cycle, which is generally limited by the nutrient supply [Falkowski, 2000].

Although we have demonstrated a potential overpressure source that could drive SGD, the magnitude of overpressure is transient due to the cycling of late Pleistocene ice sheets. Therefore, rates of SGD that may be linked to glacial overpressure likely differ between glacial and interglacial periods.

## 8. Conclusions

A low-velocity zone in smoothed interval velocities, further resolved by a full-waveform inversion, shows a distinct, localized region of low velocity that corresponds to relatively high amplitude, disturbed reflections (bright spots) in a seismic section off Massachusetts, USA. The bright spots occur in glaciogenic sediments overlying a MIS 12 glacial erosion surface (U1). By inferring effective stress from seismic velocity anomalies, we interpret a reduced velocity within the bright spots to indicate regions of localized overpressure. The results of our 1-D numerical modeling show that glacial loading and sedimentation produce overpressure, but these mechanisms alone will not produce localized overpressure around the U1 unconformity surface. By including additional overpressure sources in our 1-D model, we showed that a plausible source for localized overpressure may be the migration of overpressures through a high-permeability clinoform directly below the bright spots. Overpressure in an underlying layer may have also caused fluid expulsion and sediment deformation in the region of the bright spots. The overpressure we observed is related to a series of late Pleistocene glaciations that generated overpressure. This overpressure may contribute to SGD in the region. The connection between SGD and glaciations is also likely to contribute to the periodicity of SGD and the corresponding SGD-derived nutrient supply to the oceans.

## Appendix A: Full-Waveform Inversion Modeling

We follow the methods of Kormendi and Dietrich [1991], which apply the Fréchet derivatives of Dietrich and Kormendi [1990] and use a conjugate gradient algorithm to iteratively solve the nonlinear inverse problem. The inverse problem seeks a 1-D stratified Earth model ( $m$ ) that minimizes the cost function  $S(m)$ :

$$S(m) = \frac{1}{2} \left( \|d_{\text{syn}} - d_{\text{obs}}\|_D^2 + \|m - m_0\|_M^2 \right), \quad (\text{A1})$$

where  $d_{\text{obs}}$  is the observed CDP gather,  $d_{\text{syn}}$  is the synthetic wavefield,  $m_0$  is the starting model, and  $\| \cdot \|$  are weighted  $L^2$  norms. A fully elastic synthetic wavefield is calculated from ( $m$ ) using the reflectivity algorithm of Kennett and Kerry [1979] with layer parameters of  $P$  and  $S$  wave velocities, density, and attenuation. The

inversion scheme iteratively solves for  $P$  wave velocity updates, and  $S$  wave velocity and density are updated at each iteration based on empirical relationships [Hamilton, 1978; Castagna *et al.*, 1985; Korenaga *et al.*, 1997].

The inversion is performed in the frequency/ray parameter ( $\omega$ - $p$ ) domain. CDP gathers were first transformed to the intercept time/ray parameter ( $\tau$ - $p$ ) domain using the approach outlined in Korenaga *et al.* [1997] and then transformed to the  $\omega$ - $p$  domain using a Fourier transform. The finite aperture of the MCS streamer limits the range of ray parameters in the data, and the range limit varies as a function of  $\tau$ . We calculated the expected range of observed  $p$  as a function of  $\tau$  using a smoothed interval velocity determined from semblance analysis (Figure 4). We limited the  $p$  range of the data for three discrete  $\tau$  windows such that the maximum  $p$  included in the inversion is slightly less than the maximum expected  $p$ . For example, for the upper 0.25 s of data, where the greatest  $p$  values are present, we use a maximum  $p$  value of 0.35. This method achieves a resolution in the velocity field on the order of one fourth of the wavelength, yielding a resolution of 2–4 m given the frequency range of the seismic source used for this survey.

### A1. Source Wavelet

An accurate estimate of the source wavelet is critical for the inversion, since the cost function is based on a sample-for-sample difference of the observed and synthetic data, and the synthetic data are determined as the theoretical response of the 1-D stratified Earth model convolved with the estimated source. We follow the methods of Korenaga *et al.* [1997] and Minshull *et al.* [1994] to estimate the source wavelet using the recording of the first arrival ( $P$ ) and first multiple ( $M$ ) in the near-offset trace. The first arrival is the convolution of the source and the seafloor response function, and the recorded multiple is the negative convolution of the source with the seafloor response function twice,

$$P(t) = s(t)*r(t) \quad (A2)$$

$$M(t) = -s(t)*r(t)*r(t) \quad (A3)$$

where  $P(t)$  and  $M(t)$  are the primary and multiple time series,  $s(t)$  is the source signal,  $r(t)$  is the seafloor response function, and  $*$  denotes the convolution operator. Dividing equation (A3) by equation (A2) yields

$$r(t) = -M(t)/P(t). \quad (A4)$$

The source signal can be obtained from equations (A2) and (A4) as

$$s(t) = P(t)/r(t). \quad (A5)$$

Equations (A4) and (A5) are solved in the frequency domain. To enhance the signal of the primary and the multiple, we stack the near-offset traces from 20 adjacent shots. The exact primary and multiple traveltimes are calculated for the given water depth and source-receiver offsets and are used to window the primary and the multiple arrival times prior to deconvolution. The result of the deconvolution is then used as the source for the full-waveform inversion.

### Acknowledgments

This work was funded by NSF-OCE-0824368. Seismic data were collected on the R/V *Endeavor* (cruise EN465) using Scripps Institution of Oceanography's portable seismic system. We thank the Scripps technicians and the crew of the R/V *Endeavor* for their assistance in collecting the data. We thank Helen Feng for her help with the source deconvolution. Ingo Pecher and two anonymous reviewers provided insightful comments that improved this manuscript.

### References

- Bense, V. F., and M. A. Person (2008), Transient hydrodynamics within intercratonic sedimentary basins during glacial cycles, *J. Geophys. Res.*, 113, F04005, doi:10.1029/2007JF000969.
- Bethke, C., and T. Corbet (1998), Linear and nonlinear solution for one-dimensional compaction flow in sedimentary basins, *Water Resour. Res.*, 24, 461–467.
- Boulton, G. S., and P. Caban (1995), Groundwater flow beneath ice sheets: Part II—Its impact on glacier tectonic structures and moraine formation, *Quat. Sci. Rev.*, 14, 563–587.
- Boulton, G. S., T. Slot, K. Blessing, P. Glasbergen, T. Leijnse, and K. van Gijssel (1993), Deep circulation of groundwater in overpressured subglacial aquifers and its geologic consequences, *Quat. Sci. Rev.*, 12, 793–745.
- Bowers, G. L. (1995), Pore pressure estimation from velocity data: Accounting for overpressure mechanisms besides undercompaction, *SPE Drill. Completion*, 10(2), 89–95.
- Bowers, G. L. (2002), Detecting high overpressure, *Leading Edge*, 21, 174–177.
- Bredehoeft, J. D., and B. B. Hanshaw (1968), On the maintenance of anomalous fluid pressures: I. Thick sedimentary sequences, *Geol. Soc. Am. Bull.*, 79, 1079–1106.
- Carcione, J. M., H. B. Helle, N. H. Pham, and T. Toverud (2003), Pore pressure estimation in reservoir rocks from seismic reflection data, *Geophysics*, 68(5), 1569–1579.
- Castagna, J. P., M. L. Batzle, and R. L. Eastwood (1985), Relationships between compressional-wave and shear-wave velocities in clastic silicate rocks, *Geophysics*, 50(4), 571–581.
- Church, T. M. (1996), An underground route for the water cycle, *Nature*, 380, 579–580.
- Cohen, D. M., et al. (2010), Origin and extent of fresh paleowaters on the Atlantic continental shelf, USA, *Ground Water*, 48(1), 143–158.

- Corbet, T. F., and C. M. Bethke (1992), Disequilibrium fluid pressures and groundwater flow in the Western Canada sedimentary basin, *J. Geophys. Res.*, 97, 7203–7217.
- Dietrich, M., and F. Kormendi (1990), Perturbation of the plane-wave reflectivity of a depth-dependent elastic medium by weak inhomogeneities, *Geophys. J. Int.*, 100, 203–214.
- Domenico, S. N. (1976), Effect of brine-gas mixture on velocity in an unconsolidated sand reservoir, *Geophysics*, 41(5), 882–894.
- Dugan, B., and P. B. Flemings (2002), Fluid flow and stability of the U.S. continental slope offshore New Jersey from the Pleistocene to the present, *Geofluids*, 2, 137–146.
- Dugan, B., and T. Germaine (2008), Near-seafloor overpressure in the deepwater Mississippi Canyon, northern Gulf of Mexico, *Geophys. Res. Lett.*, 35, L02304, doi:10.1029/2007GL032275.
- Dugan, B., and T. C. Sheahan (2012), Offshore sediment overpressures of passive margins: Mechanisms, measurements, and models, *Rev. Geophys.*, 50, RG3001, doi:10.1029/2011RG000379.
- Dugan, B., P. B. Flemings, D. L. Olgaard, and M. J. Gooch (2003), Consolidation, effective stress, and fluid pressure of sediments from ODP Site 1073 U.S. mid-Atlantic continental slope, *Earth Planet. Sci. Lett.*, 215, 13–36.
- Dutta, N. C. (2002), Geopressure prediction using seismic data: Current status and the road ahead, *Geophysics*, 67(6), 2012–2041.
- Dvorkin, J., and A. Nur (2002), Critical-porosity models, in A. R. Huffman and G. L. Bowers eds., *Pressure regimes in sedimentary basins and their prediction*, AAPG Mem., 76, 33–41.
- Ecker, C., J. Dvorkin, and A. M. Nur (2000), Estimating the amount of gas hydrate and free gas from marine seismic data, *Geophysics*, 65(2), 565–573.
- Erickson, S. N., and R. D. Jarrard (1998), Velocity-porosity relationship for water-saturated siliciclastic sediments, *J. Geophys. Res.*, 103, 30,385–30,406.
- Falkowski, P. (2000), The global carbon cycle: A test of our knowledge of Earth as a system, *Science*, 290, 291–296.
- Flemings, P. B., B. B. Stump, T. Finkbeiner, and M. Zoback (2002), Flow focusing in overpressured sandstones: Theory observations, and applications, *Am. J. Sci.*, 302, 827–855.
- Fletcher, C. A. J. (1997), *Computational Techniques for Fluid Dynamics*, Fundamental and General Techniques, vol. I, Springer-Verlag, Heidelberg.
- Folger, D. W., R. A. Hathaway, R. A. Christopher, P. C. Valentine, and C. W. Poag (1978), Stratigraphic test well, Nantucket Island, Massachusetts, *US Geol. Surv. Circ.*, 773, 28.
- Gordon, D. S., and P. B. Flemings (1998), Generation of overpressure and compaction-driven fluid flow in a Plio-Pleistocene growth-faulted basin, Eugene Island 330, offshore Louisiana, *Basin Res.*, 10, 177–196.
- Green, D. H., and H. F. Wang (1986), Fluid pressure response to undrained compression in saturated sedimentary rock, *Geophysics*, 51(4), 948–956.
- Greenlee, S. M., W. J. Devlin, K. G. Miller, G. S. Mountain, and P. B. Flemings (1992), Integrated sequence stratigraphy of Neogene deposits, New Jersey continental shelf and slope: Comparison with the Exxon model, *GSA Bull.*, 104, 1403–1411.
- Hamilton, E. L. (1978), Sound velocity-density relations in sea-floor sediments and rocks, *J. Acoust. Soc. Am.*, 63(2), 366–377.
- Hart, B. S., P. B. Flemings, and A. Deshpande (1995), Porosity and pressure: Role of compaction disequilibrium in the development of geo-pressure in a Gulf Coast Pleistocene basin, *Geology*, 23(1), 45–48.
- Huffman, A. R. (2002), The future of pore-pressure prediction using geophysical methods, *Leading Edge*, 21, 199–205.
- Hutchinson, D. R., K. D. Klitgord, and R. S. Detrick (1986), Rift basins of the Long Island platform, *GSA Bull.*, 97, 688–702.
- Ingebretsen, S., W. Stanford, and C. Neuzil (2007), *Groundwater in Geologic Processes*, Cambridge Univ. Press, Cambridge U. K.
- Iverson, N., and M. Person (2012), Glacier-bed geomorphic processes and hydrologic conditions relevant to nuclear waste disposal, *Geofluids*, 12, 38–57.
- Johannes, R. E. (1980), The ecological significance of the submarine discharge of groundwater, *Mar. Geol.–Prog. Ser.*, 3, 365–373.
- Keller, C. K., G. Van Der Kamp, and J. A. Cherry (1989), A multiscale study of the permeability of a thick clayey till, *Water Resour. Res.*, 25, 2299–231.
- Kennett, B. L. N., and N. J. Kerry (1979), Seismic waves in a stratified half space, *Geophys. J. Int.*, 57, 557–583.
- Korenaga, J., W. S. Holbrook, S. C. Singh, and T. A. Minshull (1997), Natural gas hydrates on the southeastern U.S. margin: Constraints from full waveform and travel time inversions of wide-angle seismic data, *J. Geophys. Res.*, 102, 15,345–15,365.
- Kormendi, F., and M. Dietrich (1991), Nonlinear waveform inversion of plane-wave seismograms in stratified elastic media, *Geophysics*, 56(5), 644–674.
- Kristensen, T. B., J. A. Piotrowski, M. Huuse, O. R. Clausen, and L. Hamberg (2008), Timetransgressive tunnel valley formation indicated by infill sediment structure, North Sea—The role of glaciohydraulic supercooling, *Earth Surf. Processes Landforms*, 33, 546–559.
- Lemieux, J.-M., E. A. Sudicky, W. R. Peltier, and L. Tarasov (2008), Simulating the impact of glaciations on continental groundwater flow systems: 1. Relevant processes and model formulation, *J. Geophys. Res.*, 113, F02017, doi:10.1029/2007JF000928.
- Lizarralde, D., and S. Swift (1999), Smooth inversion of VSP traveltimes data, *Geophysics*, 64(3), 659–661.
- Marion, D., A. Nur, H. Yin, and D. H. Han (1992), Compressional velocity and porosity in sand-clay mixtures, *Geophysics*, 57(4), 554–563.
- Marksamer, A. J., M. Person, F. Day-Lewis, J. W. Lane, D. Cohen, B. Dugan, H. Kooi, and M. Willett (2007), Integrating geophysical, hydrochemical, and hydrologic data to understand the freshwater resources on Nantucket Island, Massachusetts, in *Subsurface Hydrology Data Integration in Subsurface Hydrology*, edited by D. W. Hyndman, F. D. Day-Lewis, and K. Singha, pp. 1–54, AGU, Washington D. C.
- Mavko, G., T. Mukerji, and J. Dvorkin (2009), *The Rock Physics Handbook*, Cambridge Univ. Press, Cambridge, U. K.
- Minshull, T. A., S. C. Singh, and G. K. Westbrook (1994), Seismic velocity structure at a gas hydrate reflector, offshore western Colombia, from full waveform inversion, *J. Geophys. Res.*, 99, 4715–4734.
- Moore, W. S. (2010), The effect of submarine groundwater discharge on the ocean, *Annu. Rev. Mar. Sci.*, 2, 59–88.
- Moore, W. S., J. L. Sarmiento, and R. M. Key (2008), Submarine groundwater discharge revealed by  $^{228}\text{Ra}$  distribution in the upper Atlantic Ocean, *Nat. Geosci.*, 1, 309–311.
- Morgan, E. C., M. Vanneste, I. Lecomte, L. G. Baise, O. Longva, and B. McAdoo (2012), Estimation of free gas saturation from seismic reflection surveys by the genetic algorithm inversion of P-wave attenuation model, *Geophysics*, 77, R175–R187, doi:10.1190/GEO2011-0291.1.
- Oldale, R. N., and C. J. O'Hara (1984), Glaciectonic origin of the Massachusetts coastal end moraines and a fluctuating late Wisconsinan ice margin, *GSA Bull.*, 95, 61–74.
- Person, M., B. Dugan, J. Swenson, L. Urbano, C. Stott, J. Taylor, and M. Willett (2003), Pleistocene hydrogeology of the Atlantic continental shelf, New England, *Geol. Soc. Am. Bull.*, 115, 1324–1343.
- Person, M., J. McIntosh, V. Bense, and V. H. Remenda (2007), Pleistocene hydrology of North America: The role of ice sheets in reorganizing groundwater flow systems, *Rev. Geophys.*, 45, RG3007, doi:10.1029/2006RG000206.
- Person, M., A. Marksamer, B. Dugan, P. E. Sauer, K. Brown, D. Bish, K. J. Licht, and M. Willett (2012), Use of a vertical  $\delta^{18}\text{O}$  profile to constrain hydraulic properties and recharge rates across a glacio-lacustrine unit, Nantucket Island, *Hydrogeol. J.*, 20, 325–336.

- Phrampus, B. J., and M. J. Hornbach (2012), Recent changes to the Gulf Stream causing widespread gas hydrate destabilization, *Nature*, **490**, 527–530, doi:10.1038/nature11528.
- Roberts, S. J., and J. Nunn (1995), Episodic fluid expulsion from geopressured sediments, *Mar. Pet. Geol.*, **12**, 195–204.
- Sain, K., T. A. Minshull, S. C. Singh, and R. W. Hobbs (2000), Evidence for a thick free gas layer beneath the bottom simulating reflector in the Makran accretionary prism, *Mar. Geol.*, **164**, 3–12.
- Sayers, C. M., G. M. Johnson, and G. Denyer (2002), Predrill pore-pressure prediction using seismic data, *Geophysics*, **67**(4), 1286–1292.
- Siegel, J., D. Dugan, D. Lizarralde, M. Person, W. DeFoos, and N. Miller (2012), Geophysical evidence of a late Pleistocene glaciation and paleo-ice stream on the Atlantic Continental Shelf offshore Massachusetts, USA, *Mar. Geol.*, **303–306**, 63–74.
- Slomp, C. P., and P. V. Cappellen (2004), Nutrient inputs to the coastal ocean through submarine groundwater discharge: Controls and potential impact, *J. Hydrol.*, **295**, 64–86.
- Steckler, M. S., G. S. Mountain, K. G. Miller, and N. Christie-Blick (1999), Reconstruction of Tertiary progradation and clinoform development on the New Jersey passive margin by 2-D backstripping, *Mar. Geol.*, **154**, 399–420.
- Stigall, J., and B. Dugan (2010), Overpressure and earthquake initiated slope failure in the Ursa region, northern Gulf of Mexico, *J. Geophys. Res.*, **115**, B04101, doi:10.1029/2009JB006848.
- Swarbrick, R. E., and M. J. Osborne (1998), Mechanisms that generate abnormal pressures: An overview, in *Abnormal Pressures in Hydrocarbon Environments*, vol. 70, edited by B. E. Law, G. F. Ulmishek, and V. I. Slavin, pp. 13–34, AAPG Memoir, Tulsa, Okla.
- Taylor, M. H., W. P. Dillon, and I. A. Pecher (2000), Trapping and migration of methane associated with the gas hydrate stability zone at the Blake Ridge Diapir: New insights from seismic data, *Mar. Geol.*, **164**, 79–89.
- Uchupi, E., N. Driscolla, R. D. Ballardb, and S. T. Bolmer (2001), Drainage of late Wisconsin glacial lakes and the morphology and late quaternary stratigraphy of the New Jersey-southern New England continental shelf and slope, *Mar. Geol.*, **172**, 177–145.
- Virieux, J., and S. Operto (2009), An overview of full-waveform inversion in exploration geophysics, *Geophysics*, **74**(6), 1–26.
- White, J. E. (1975), Computed seismic speeds and attenuation in rocks with partial gas saturation, *Geophysics*, **40**, 224–232, doi:10.1190/1.1440520.
- Xu, W., and C. Ruppel (1999), Predicting the occurrence, distribution, and evolution of methane gas hydrate in porous marine sediments, *J. Geophys. Res.*, **104**, 5081–5095.
- Yardley, G. S., and R. E. Swarbrick (2000), Lateral transfer: A source of additional overpressure?, *Mar. Petroleum Geol.*, **17**, 523–537.